Nature Communications

Article in Press

Interfacial evaporation-induced localized multi-field coupling enables efficient co-recovery of freshwater and nitrates

Zhen Yu, Lei Shi, Ruibin Ning, Haobin Huang, Zhiqiang Sun, Jiajun Chen, Tian Zhou & Swee Ching Tan

We are providing an unedited version of this manuscript to give early access to its findings. Before final publication, the manuscript will undergo further editing. Please note there may be errors present which affect the content, and all legal disclaimers apply.

If this paper is publishing under a Transparent Peer Review model then Peer Review reports will publish with the final article.

Interfacial evaporation-induced localized multi-field coupling enables efficient co-recovery of freshwater and nitrates

Zhen Yu[1, #], Lei Shi[2, #, *], Ruibin Ning[2], Haobin Huang[3], Zhiqiang Sun[2], Jiajun Chen[2], Tian Zhou[2], Swee Ching Tan[1,*]

1 Department of Materials Science and Engineering, National University of Singapore, Singapore 117574, Singapore

2 School of Energy Science and Engineering, Central South University, Changsha 410083, China

3 State Key Laboratory of Applied Microbiology Southern China, Institute of Microbiology, Guangdong Academy of Sciences, Guangzhou 510070, China

# These authors contributed equally to this work.

* Corresponding authors: shi.lei@csu.edu.cn; msetansc@nus.edu.sg

Abstract

Recovering nitrate from surface water can alleviate the intertwined environmental, resource, and energy challenges. In response, we have developed a bioinspired photothermal evaporation platform (BPEP) for the efficient co-recovery of low-concentration nitrate and freshwater. Through the evaporation-induced localized multi-field (flowing, concentration, temperature) enhancement effect, the BPEP achieves a high nitrate recovery capacity of 8510 g m^{-2} under 1 sun illumination, approximately 6.7 times that under dark conditions. The flowing field is identified as the dominant contributor, accounting for nearly 80% of the total enhancement. In outdoor testing, BPEP demonstrates a high nitrate recovery of around 25.9 mg m^{-2}, with a daily water collection rate of about 8.46 kg m^{-2}. The extracted nitrate by BPEP can be further converted into nitrogen fertilizer *via* catalytic processes, thereby promoting plant growth. BPEP thus provides an integrated strategy to recover nitrate and freshwater, addressing pressing issues in global sustainable development.

Introduction

Freshwater shortages and food crises are intertwined global challenges, as highlighted in Sustainable Development Goals 2 and 6[1-3]. With the world's population growing and climate change intensifying continuously, countries and regions face varying degrees of water and food crises (Supplementary Fig. 1). It is thus crucial to address the above issues by integrating multidisciplinary approaches or formulating effective policy frameworks, thereby ensuring the sustainable use of water resources and the stability of food production[4-7]. Nitrate, a substance that embodies both resource value and environmental pollution, is widely distributed in natural environments[8,9]. Specifically, nitrate plays a crucial role in industry, agriculture, and natural ecosystems[10,11], but improper use or excessive discharge will lead to various environmental and health problems (Supplementary Fig. 2)[12,13]. At present, nitrate production predominantly relies on traditional energy-intensive processes, including ammonia synthesis (Haber-Bosch process) and ammonia oxidation (Ostwald process)[14]. These processes necessitate high temperatures and pressures, resulting in substantial energy consumption and greenhouse gas emissions[15,16]. Therefore, efficient recovery and reintegration of nitrates into the industrial cycle or agricultural utilization could help mitigate water pollution and reduce synthesis energy demands[17-19].

Recently, various innovative designs for high-concentration nitrate recovery and upgrading have emerged, including electrocatalysis, electrodialysis, reverse osmosis, ion exchange, adsorption, and biological treatment[20-22]. For example, a layered double hydroxide/copper foam hybrid electrocatalyst can effectively reduce nitrate to ammonia under mild conditions, achieving an impressive conversion rate of 98.5%[23]. Additionally, a porous carbon film derived from eggshell biowaste can selectively adsorb nitrate under an electric field, with a maximum nitrate adsorption capacity of 2.4×10^{-3} mmol m^{-2} [24]. However, recovering low-concentration nitrates from surface water remains a significant challenge due to cost and energy consumption. Meanwhile, these technologies are limited to removing single pollutants, which cannot yet transform complex and contaminated water bodies into clean water or safe water sources for human use. Developing processes that can simultaneously recover nitrates and purify water remains a significant challenge.

Interfacial solar-driven evaporation technology is an emerging energy conversion approach that enables efficient solvent evaporation under ambient conditions by localizing heat at the gas-liquid interface[25,26]. This technology holds significant promise for applications in seawater desalination, wastewater treatment, medical sterilization, and other fields[27-29]. In response to the escalating energy-resource-environment trilemma, recent research has shifted toward integrated water resource recovery[30,31], where interfacial evaporation systems coupled with selective adsorbents can simultaneously extract water molecules and valuable ions (e.g., lithium ion, uranium ion). Unlike conventional adsorption methods, interfacial solar-driven evaporation technology eliminates energy-intensive pretreatment steps, enabling direct solar-powered enrichment of low-concentration target ions and making it promising for the co-extraction of low-concentration nitrate from surface water. The key challenge lies in developing high-performance adsorbents that balance photothermal conversion and selective nitrate capture. Traditional nitrate adsorbents, such as kaolin[32], zeolite[33], ion-exchange resins[34], and modified chitosan[35], suffer from poor light absorption and complex synthesis, whereas broad-spectrum adsorbents like activated carbon exhibit low selectivity and weak adsorption capacity[36,37]. Thus, selecting advanced adsorbents that combine high photothermal efficiency with targeted nitrate affinity is critical. Among potential candidates, polypyrrole (PPy) stands out due to its unique performance advantages[38].

Some sun-loving plants exhibit a marked light-dependent nitrate adsorption behavior, that is, slower nitrate adsorption kinetics in the dark than under illumination[39]. Inspired by this, we develop a bioinspired photothermal nitrate recovery platform (BPEP, Fig. 1a). Because PPy can grow controllably on various substrates through a simple self-assembly process[40], we fabricate a polypyrrole-coated bacterial cellulose hydrogel (BCBH/PPy) *via* in situ polymerization. Compared to conventional substrates, hydrogel-based evaporators offer reduced evaporation enthalpy, potentially surpassing thermodynamic limits, while BCBH's freeze-drying-free synthesis ensures scalability[41]. Owing to these advantages, we demonstrate the performance of BPEP by using BCBH/PPy as a model material. To the best of our knowledge, BPEP demonstrates a previously unexplored design for simultaneously recovering clean water and nitrate. The BPEP

can enhance nitrate recovery through evaporation-induced multi-field (temperature, flowing, and concentration) under solar irradiation (Fig. 1b). Specifically, the thermal localization design of BPEP induces distinct temperature and concentration gradient distributions from the evaporation interface to the bulk solution (Figs. 1b-I and II). Compared to the initial conditions, the localized concentration and temperature fields synergistically enhance nitrate adsorption (Figs. 1b-I and II), as evidenced by both kinetic and thermodynamic analyses. Furthermore, the evaporation process accelerates the transport of nitrate ions in both the top and bottom layers of BPEP (Figs. 1b-III), thereby increasing the collision probability between nitrate anions and adsorption sites. Due to its selective adsorption properties, BPEP exhibits a strong affinity for nitrate ions while showing limited capture efficiency for other competing ions. The above mechanisms will be elaborated in detail in the following sections. The potential to convert nitrates into harmless substances or high-value products through biochemical or catalytic reactions is also demonstrated. These results position BPEP as a promising platform for addressing the water-food-energy nexus by integrating with existing treatment technologies.

Results and Discussion

Fabrication and characterization

The main functional component of BPEP was BCBH/PPy, which served as a light-absorber and nitrate adsorbent. BCBH/PPy was prepared by a simple fermentation and in-situ coating method (Fig. 2a)[41]. After purification, bacterial cellulose hydrogel (BCBH) showed a loose, porous structure composed of cellulose fibers with diameters ranging from 30~50 nm. These pores served as transport channels for water, vapor, and salt ions (Fig. 2b). Meanwhile, these interlocked cellulose fibers endowed the excellent mechanical properties of BCBH (Supplementary Fig. 3). In comparison, the structure of BCBH/PPy showed minimal changes, with numerous nanoparticles on the fibers (Fig. 2c). BCBH/PPy also demonstrated excellent hydrophilicity (Supplementary Fig. 4). Although X-ray diffraction (XRD) spectra indicated little difference between the BCBH and BCBH/PPy (Fig. 2d), the X-ray photoelectron spectroscopy (XPS) survey revealed the presence

of nitrogen element in BCBH/PPy at a binding energy of approximately 399.8 eV (Fig. 2e). The functional groups of BCBH and BCBH/PPy were further characterized by Raman spectra (Fig. 2f). The typical band at 1588 cm^{-1} corresponded to the symmetric stretching mode of the C=C skeletal structure, absent in the pyrrole (Py) monomer[42-44]. The peak at 1336 cm^{-1} represented the PPy ring-stretching mode[45-47]. These findings collectively verified the successful coating of PPy on BCBH. The structural diagram of BPEP was shown in Supplementary Fig. 5. BCBH/PPy, as the absorber in the BPEP, held a high average optical absorption of around 97% across the full solar spectrum (Fig. 2g). The selective adsorption mechanism of nitrate by BCBH/PPy will be discussed in detail below. The evaporation performance of BPEP was evaluated using a custom device (Supplementary Fig. 6). As the solar flux increased from 0.6 suns to 1.2 suns, the steady-state temperature of the BPEP surface rose from 39.4 to 44.8°C (Fig. 2h), while the bottom water remained at a low temperature (Fig. 2h and Supplementary Fig. 7). The excellent heat localization capability of BPEP can be attributed to its physical thermal insulation layer (polystyrene foam). This structure effectively suppresses heat conduction into the bulk water, confining thermal energy mainly to the gas-liquid interface. The COMSOL simulation verified the heat localization design (Supplementary Fig. 8). As a result, the most absorbed heat is utilized for steam generation rather than being dissipated as sensible heat in the water[48], thereby achieving high-efficiency evaporation under solar irradiation. Note that the surface temperature of dry BCBH/PPy rapidly exceeded 80°C under 1 sun illumination (Supplementary Fig. 9), demonstrating excellent photothermal conversion. A thermos-gravimetric analysis (TGA) was conducted to examine the contents of BCBH and BCBH/PPy components, as well as their transformation processes (Supplementary Fig. 10). The carbonization of BCBH/PPy began at approximately 300 ˚C and ended at around 560 ˚C, demonstrating that BCBH/PPy remained thermally stable during the evaporation process.

Solar-driven co-recovery performance

Fig. 3a showed that BCBH/PPy presented a higher stable temperature of 45.7°C over pure water and BCBH under 1.2 sun. Meanwhile, the evaporation rate of BCBH/PPy was 2.01 kg m^{-2} h^{-1}, *ca* 3.7 and 1.7 times that of pure water and BCBH, respectively (Fig. 3b). As the solar flux increased

from 0.6 sun to 1.2 sun, the evaporation rate increased from 1.12 to 2.01 kg m^{-2} h^{-1} (Fig. 3c). The impressive evaporation rate can be attributed to the low evaporation enthalpy of BCBH/PPy (Supplementary Fig. 11). BCBH/PPy contains numerous hydrophilic groups that engage in noncovalent interactions with water molecules through hydrogen bonding and electrostatic repulsion, significantly enhancing the content of intermediate water and reducing evaporation enthalpy[31]. Raman spectroscopy was employed to confirm this hypothesis (Fig. 3d), revealing the presence of free water and intermediate water in BCBH/PPy, with a ratio of 1.7. Unless otherwise specified, BPEP will refer to BPEP based on BCBH/PPy.

We next evaluated the nitrate adsorption performance of BPEP under 1 sun illumination. Notably, BPEP exhibited significantly enhanced adsorption capacity under light irradiation compared to dark conditions (Fig. 3e), regardless of whether BCBH or BCBH/PPy was employed as the absorber. Specifically, when utilizing BCBH/PPy as the photothermal absorber, BPEP achieved a remarkable nitrate adsorption capacity of 8510 g m^{-2} under 1 sun illumination, approximately 6.7 times that observed in the dark (Fig. 3e). Furthermore, as the solar flux was intensified from 0.6 to 1.2 suns, the nitrate adsorption performance demonstrated from 7111 to 9318 g m^{-2} (Fig. 3f). We further excluded the effect of different ions on the nitrate adsorption performance. The results showed that common ions had little effect on the nitrate adsorption capacity of BPEP (Supplementary Fig. 12). BPEP can maintain a high adsorption capacity of at least 5908 g m^{-2} at different pH values (Supplementary Fig. 13). The cyclic adsorption experiment revealed that after 10 cycles, BPEP still retained approximately 80% of its initial nitrate adsorption capacity (Fig. 3g). Meanwhile, the UV-Vis spectrum of the post-10th cycle solution revealed no significant absorbance differences compared to the initial nitrate solution (Supplementary Fig. 14), also demonstrating the good cyclic stability of BCBH/PPy.

The actual nitrate recovery performance of BPEP was validated through outdoor experiments. The outdoor experiments used water from an urban river, with sampling sites located at 114.1°E and 22.5°N, as shown in Supplementary Fig. 15. The outdoor setup was depicted in Supplementary Fig. 16. The outdoor device's top layer is constructed with an acrylic sheet, enabling over 95%

transmittance to minimize light loss (Supplementary Fig. 17). The evaporation performance of BPEP outdoors was generally positively correlated with solar flux, with the maximum evaporation rate reaching 1.35 kg m^{-2} h^{-1} (Fig. 3h). The daily water collection rate (WCR) of the outdoor device was 8.46 kg m^{-2}, and the daily water collection efficiency (WCE) was about 72.1% (Fig. 3i). After one day of outdoor testing, BPEP could reduce the nitrate concentration in an urban river from 33.7 to 1.1 mg L^{-1}, with the corresponding nitrate recovery of around 25.9 mg m^{-2} (Supplementary Fig. 18). Note that the nitrate recovery capacity of BPEP outdoors was significantly lower than that under 1 sun indoors, which can be attributed to the lower nitrate concentration in surface water. The economic performance of BPEP was evaluated (The details can be found in Supplementary Note 1). The fabrication cost of BPEP was 5.39 $ m^{-2}, with the cost efficiency of BPEP about 2.99 $ h kg^{-1}.

In addition, BPEP can also desalinate seawater and treat wastewater. Thanks to the effective salt transfer properties (Supplementary Fig. 19) and intermittent operation mode[40,48,49], BPEP enabled stable evaporation of seawater over 15 cycles (Supplementary Fig. 20). The obtained distilled water meets the drinking water limit stipulated by the World Health Organization (WHO) (Supplementary Fig. 21). The intermittent operation design theoretically allowed BPEP unlimited use in seawater, provided that the BCBH/PPy degradation was not considered. For higher-concentration brine, BPEP's average evaporation performance would be degraded. Taking NaCl solution as an example, when the concentration rose to 20 wt%, the evaporation rate of BPEP decreased from 1.77 to 1.65 kg m^{-2} h^{-1} (Supplementary Table 1). The evaporation enthalpy of BPEP also decreased from 1.83 to 1.64 MJ kg^{-1} with increasing salinity (Supplementary Table 1), consistent with the reported work[50]. According to Eq. (2), this reduction directly contributed to the decline in evaporation efficiency (Supplementary Table 1). Nevertheless, it is essential to emphasize that BPEP primarily targets eutrophic surface water, where salinity typically remains below 3.5 wt%. Under these realistic conditions, BPEP maintains excellent evaporation performance. Additionally, BPEP demonstrated effective purification in industrial dyeing wastewater and urban domestic sewage. Specifically, the removal ratios of chemical oxygen

demand (COD), total organic carbon (TOC), and total dissolved solids (TDS) all exceeded 99% (Supplementary Table 2). In brief, the above results showed that BPEP can produce clean water from actual water sources (e.g., surface water, seawater, practical wastewater, etc.).

Mechanism for enhanced nitrate recovery

The enhanced nitrate recovery performance of BPEP mainly resulted from the selective adsorption properties of the PPy coating and the multi-field effects generated by the interfacial evaporation process, with the underlying mechanisms as follows:

(1) Nitrate-selective adsorption mechanism of PPy coating: The adsorption process was mainly governed by electrostatic interaction and hydrogen bonding. Density functional theory (DFT) calculations showed an adsorption energy of -0.34 eV for nitrate on PPy, confirming the thermodynamic spontaneity of the adsorption process (Fig. 4a). Note that PPy existed as a three-dimensional structure in the DFT calculation, allowing for the spontaneous adsorption of nitrate ions at multiple accessible sites (Supplementary Fig. 22). XPS spectra further confirmed the adsorption mechanism. Before adsorption, the N1s peak at 399.8 eV (Fig. 4b) was associated with benzenoid amine (-NH-)[51]. After nitrate adsorption, the novel N1s peaks at 406.7 eV (Fig. 4c), corresponding to the nitrate[52]. Moreover, the decrease and shift in the binding energy of benzenoid amine suggested that this group was responsible for nitrate adsorption. The adsorption mechanism likely involved electrostatic attraction or coordination between the functional groups and nitrate[24,53]. The O1s peak for initial BCBH/PPy at 532.6 eV (Fig. 4c) was indexed to -OH[54]. After nitrate adsorption, the O1s spectrum showed a novel peak at 530.5 eV (Fig. 4c), corresponding to the C=O, probably attributed to the redistribution of electron clouds in PPy molecules [55]. Meanwhile, the -OH functional group contents were lower than those before adsorption, indicating that hydrogen bonds were formed during the adsorption process[38]. The dual adsorption mechanism of the PPy coating synergistically enhances the nitrate-selective recovery efficiency.

(2) Evaporation-induced flowing field. The interfacial evaporation process significantly enhances ion transport within the BPEP system, increasing the collision frequency between target nitrate ions and active adsorption sites. To quantify this effect, we performed COMSOL simulations

comparing the spatial distribution of nitrate concentrations in the BPEP absorber under 1-sun illumination with dark conditions (simulation details are provided in the Supplementary Information). As demonstrated in Figure 4d-I, solar-driven evaporation significantly enhances BPEP's nitrate adsorption capacity, with a maximum increase of 5.2 times at the extract sampled location compared to the dark conditions (Figure 4d-II). From a kinetic perspective, interfacial evaporation generates localized temperature and concentration gradients at the gas-liquid interface, triggering the Marangoni effect. This phenomenon induces microvortices that disrupt the static diffusion boundary layer, enabling continuous delivery of nitrate ions to adsorption sites while minimizing mass-transfer resistance. Consequently, the nitrate concentration within BPEP exhibits a distinct gradient along the flow direction (Figure 4d-II).

(3) Evaporation-induced localized concentration field. Interfacial evaporation drives the preferential escape of water molecules at the gas-liquid interface, leading to a significant accumulation of target ions (nitrate ions) in the evaporation region. Thermodynamically, adsorption represents a redistribution equilibrium of solutes (nitrate ions) between the solution phase and the adsorbent interface, governed by the mass action law. Consistent with Le Chatelier's principle, an increase in bulk ion concentration shifts the equilibrium toward adsorption, as the system responds by enhancing adsorption capacity to push the equilibrium toward adsorption. Our experiments demonstrated the above regulatory mechanism: under dark conditions, elevating the initial nitrate concentration from 25 to 150 mg L^{-1} improved BPEP's adsorption capacity by ~8 times (Fig. 4e). Kinetically, the adsorption rate is governed by ion mass transfer from the bulk phase to the interface. The evaporation-sustained high-concentration microenvironment circumvents the dilution-induced mass transfer limitations inherent to conventional adsorption systems. Fick's first law further elucidates this process, defining the diffusion flux (J) as Eq. (1) where D was the diffusion coefficient; and the $\frac{dC}{dx}$ was the concentration gradient. This gradient-driven enhancement in diffusion kinetics accelerated adsorption dynamics.

$$J = -D\frac{dC}{dx} \qquad (1)$$

Both the temperature and the nitrate concentration at the evaporation interface increased under

solar illumination. In Figs. 4e and 4f, the conditions at the evaporation interface before illumination were marked as point I, whereas those after illumination were marked as point II. After 12 h of illumination under 1 sun, the nitrate concentration at the evaporation interface (point II in Fig. 4e) was approximately 2.3 times that of the initial concentration (point I in Fig. 4e), whereas the corresponding nitrate adsorption capacity increased by only 1.9 times. Considering that the nitrate adsorption capacity of BPEP under 1 sun illumination is about 6.7 times greater than that in the dark (Fig. 3e), it can be concluded that the concentration field is not the dominant factor contributing to the enhanced nitrate recovery under solar irradiation.

(4) Evaporation-induced localized temperature field. Due to the thermal localization design, the top temperature of BPEP is relatively high (~43.1°C under 1 sun). Increasing the temperature can appropriately improve the adsorption capacity, rising from 1289 g m^{-2} (point I in Fig. 4f) to 1458 g m^{-2} (point II in Fig. 4f). Therefore, the concentration field is not the dominant factor contributing to the enhanced nitrate recovery under solar irradiation, either. From a kinetic view, elevating the temperature enhances nitrate adsorption through two key mechanisms: (A) The Stokes-Einstein equation predicts that higher temperatures substantially decrease solution viscosity while increasing the diffusion coefficient of ions, thereby accelerating their transport to adsorption sites. (B) Simultaneously, the elevated temperature reduces the thickness of the diffusion boundary layer (δ), further improving mass transfer efficiency. Thermodynamically, an increase in temperature lowers the activation energy barrier, particularly benefiting ion exchange processes. Although the direct impact of temperature rise on nitrate adsorption capacity may appear limited, it's crucial to emphasize that solar irradiation effects generate not just a localized temperature field but also induce coupled flowing and concentration fields at the interface.

In brief, the synergistic interaction of these multiple fields (flowing, concentration, and temperature) creates a dynamic adsorption environment, thus leading to a remarkable improvement in nitrate adsorption kinetics. The contribution ratios of the localized temperature field, concentration field, and flowing field can be calculated using Eqs. (9) and (10)[26,27], which yield values of 3.2%, 20.5%, and 76.3%, respectively (Fig. 4g). The calculated details are provided

in the Supplementary Information. Note that BCBH/PPy was used as a concept proof to examine the performance and mechanism of BPEP here. To verify the universality of BPEP's structure feature and nitrate recovery mechanism, we used six reported nitrate adsorbents to fabricate BPEP. The sources of these adsorbents can be found in the legend to Fig. 4h. The fabricated details were provided in the Supplementary Information. The BPEP without any nitrate adsorbent loading exhibited negligible nitrate adsorption capability. As expected, solar irradiation significantly improved nitrate adsorption across all tested materials (Fig. 4h). These findings confirm that our proposed multi-field synergy effect is broadly applicable to diverse nitrate adsorbents, further underscoring its theoretical innovation and general relevance.

Finally, the nitrate recovery capacity of BPEP decreased by approximately 90% in 20 wt% NaCl solution. The nitrate adsorption by BCBH primarily relies on electrostatic interactions and hydrogen bonding. Since both Cl^- and NO_3^- are anions, they compete for adsorption sites on the PPy surface. Consequently, in high-concentration NaCl solutions (e.g., 20 wt%), BPEP is indeed ineffective due to overwhelming Cl^- competition. However, BPEP maintains over 90% nitrate adsorption efficiency in ~3.5 wt% NaCl solutions (Supplementary Fig. 12), which aligns well with its intended application for nitrate recovery from surface water (typically <3.5 wt% salinity). To enhance applicability in extreme environments, future work can focus on developing advanced nitrate adsorbents with increased tolerance to high salinity.

Discussion

Some issues need further discussion:

(1) Our work focuses on developing a composite system that can simultaneously produce freshwater and recover nitrate, which has not been reported before to our knowledge. Currently, we have utilized a two-dimensional (2D) evaporation structure to validate our design. To explain the higher evaporation rate of 2D-BPEP compared to the thermodynamic limit, we employed the reduced evaporation enthalpy hypothesis here. Note that some recent studies show that evaporation enthalpy may be intrinsically thermodynamically invariant[56,57]. We fully acknowledge the open

mechanism, but conclusively addressing this issue demands in situ molecular-level evidence, which exceeds the scope of our work. The primary objective of this work is not to resolve the fundamental debate on evaporation thermodynamics. By focusing on the practical implications, we aim to advance sustainable resource recovery technology while inviting the broader research community to further investigate its mechanisms.

Additionally, developing a three-dimensional (3D) evaporation structure (Supplementary Fig. 23) can further increase the evaporation rate. Specifically, after 60 minutes of 1 sun illumination, the temperature increase in the bottom water for BPEP with three-dimensional evaporation structures (3D-BPEP) was less than that of pure water and BPEP with 2D evaporation structures (2D-BPEP) (Supplementary Fig. 24). This suggests that 3D-BPEP exhibited better heat localization with reduced heat loss[48,58]. Therefore, benefiting from the above effect, along with environmental energy effect and larger evaporation area, 3D-BPEP demonstrated improved evaporation performance (Supplementary Fig. 25)[59,60]. Regarding nitrate recovery performance, we systematically evaluated 3D-BPEP at various tilt angles (Supplementary Table 3). The experimental data demonstrated a significant improvement in nitrate recovery capacity with increasing angle of 3D-BPEP. Meanwhile, 3D-BPEP consistently outperformed 2D-BPEP across all tested angles, further validating the advantages of the 3D design. Since evaporation-induced multi-field (including thermal, concentration, and flowing fields) coupling effect can promote nitrate adsorption, the improved evaporation performance of 3D-BPEP further amplifies these multi-field effects, thereby increasing the nitrate adsorption capacity. The detailed mechanism may involve a complex balance between the multi-field interactions and the intrinsic properties of the adsorbent. However, exploring this mechanism in depth is beyond the scope of the present study and will be addressed in future work. In brief, the 3D-BPEP demonstrates superior evaporation performance compared to many reported solar evaporators (Supplementary Table 4). Note that the conventional evaporation and crystallization process cannot produce the pure nitrate owing to the pollution of other co-existing matters. More importantly, because nitrate concentrations in surface water are typically low, little nitrate can be recovered by simple evaporation. In comparison, BPEP

uniquely enables the simultaneous recovery of clean water and nitrate, a capability absent in previous evaporators (Supplementary Table 4).

(2) By recovering nitrate from wastewater or surface water through BPEP, we can fully leverage the dual nature of nitrate as both a pollutant and a resource (Fig. 5a). The nitrate in BPEP can be desorbed by KCl solution and converted into KNO_3. From a pollution control perspective, the as-obtained KNO_3 can be converted into N_2 through biochemical processes such as denitrification[61]. Specifically, after 12 h of reaction in the sequencing batch reactor, the nitrate extracted by BPEP could be degraded entirely (Fig. 5b). From a resource perspective, high-concentration potassium nitrate can be used directly for phase change energy storage and fertilizer; and also employed as raw materials for bulk chemical processes, drug synthesis, and fuel production[62-64]. These nitrates can be converted into various chemicals, such as ammonia and urea, through advanced photo-, electric-, and bio-catalytic processes[65-67]. Note that the above catalytic process yields less at low nitrate concentrations[68,69]. Integrating these technologies with BPEP can address this challenge by the adsorption-enrichment-recycling process of BPEP. As an example, in the electrochemical method (details provided in the Supplementary Information), as the nitrate concentration increased from 50 to 400 mg L^{-1}, the ammonia yield rate nearly increased sevenfold (Fig. 5c and Supplementary Table 5), with the nitrate conversion ratio also improving. This demonstrates that increasing the nitrate concentration via BPEP effectively enhances nitrate conversion. It is well known that ammonia can accelerate plant growth. We used the ammonia solution to irrigate *Pakchoi* to demonstrate the practical application of the fabricated ammonia (Details can be found in Supplementary Information). We monitored the growth over 14 days, comparing *Pakchoi* irrigated with the fabricated ammonia solution or deionized water. The addition of the fabricated ammonia solution resulted in improved growth (Fig. 5d and Fig. 5e). After 14 days, the height of the *Pakchoi* with the addition of ammonia solution reached 7.15 cm, while the height of those without the ammonia solution was only 4.35 cm (Fig. 5d). These results indicate that the fabricated ammonia can be effectively used as a fertilizer. Note that the above conversion of nitrate in BPEP to nitrogen or ammonia involved two entirely different processes: the biochemical conversion to

nitrogen via denitrification, and the electrochemical reduction to ammonia. These two processes did not interfere with each other since they are different systems. The specific conversion process should be flexibly selected according to practical requirements. Overall, BPEP not only addresses nitrate pollution but also facilitates the resource utilization of nitrates in wastewater and surface water through an optimal integration of modern technologies, thereby accelerating progress towards the Sustainable Development Goals.

Methods

Preparation of BCBH and BCBH/PPy

The preparation procedure of BCBH/PPy and BCBH was illustrated in Fig. 2a. BCBH was obtained by incubating glucosacetic xylose in a fermentation medium at 30°C for 4-7 days[41]. After fermentation, the resulting BCBH was washed with deionized water until the pH reached 7 and then stored for later use. BCBH/PPy was obtained by polymerizing Py on BCBH[40,70]. Typically, 2.28 g of ammonium persulphate (APS) and 0.7 mL of Py were separately dispersed in 100 mL of deionized water to form solution A and solution B, respectively. A piece of BCBH (20 cm^2) was placed in a culture dish, followed by the addition of 10 mL of solution A and 5 mL of solution B. After reacting at 4 °C for 24 h, the resulting BCBH/PPy was thoroughly washed with deionized water to obtain the final product.

Solar-driven evaporation measurement

The structural diagram of BPEP was shown in Supplementary Fig. 5. BCBH/PPy was the absorber of BPEP. The experimental setup for solar-driven evaporation was shown in Supplementary Fig. 6. From Supplementary Fig. 26, it can be concluded that the output spectrum of solar simulator with an AM 1.5 G filter closely matched the standard AM 1.5G solar spectrum. The evaporation rate was determined by measuring the mass change of the BPEP over time. The evaporation efficiency was calculated based on the Eq. (2)[71,72] where $\dot{m}$ was the evaporation rate (kg m^{-2} h^{-1}); h_{lv} was the enthalpy change of liquid to vapor (sensible heat and evaporation enthalpy) (MJ kg^{-1}); and q_{solar} was the solar flux (kW m^{-2}).

$$\eta = \frac{\dot{m} \cdot h_{lv}}{q_{solar}} \tag{2}$$

The enthalpy change (h_{lv}) of liquid to vapor was calculated based on Eq. (3) where h_{ee} was the evaporation enthalpy obtained by DSC measurements (MJ kg^{-1}) and h_{sh} was the sensible heat (MJ kg^{-1}).

$$h_{lv} = h_{ee} + h_{sh} \tag{3}$$

The evaporation enthalpy (h_{ee}) could be calculated with the Eq. (4)[73,74] where E_s was the specific energy (MJ kg^{-1}); m_t was the total mass of the measuring sample (g); m_w was the mass of water in the measuring sample (g).

$$h_{ee} = \frac{E_s \cdot m_t}{m_w} \tag{4}$$

The specific energy (E_s) could be calculated by the integral value of specific power and time, which was equal to the integral area in Supplementary Fig. 11.

The sensible heat (h_{sh}) could be calculated by Eq. (5) where $C_{p,l}$ was the heat capacity of the bulk solution (J K^{-1} g^{-1}); T_0 was the initial temperature of the bulk solution (K); T_1 was the steady-state temperature of the bulk solution (obtained from Fig. 2h and Supplementary Fig. 7).

$$h_{sh} = \int_{T_0}^{T_1} C_{p,l} \, \mathrm{d}T \tag{5}$$

Outdoor experiments were conducted at the Central South University. The solar flux and evaporation rate were manually recorded from 8:00 a.m. to 5:00 p.m. The mass loss of BPEP was recorded every 1 h to calculate the outdoor evaporation rate. The water at the device's bottom was weighed to calculate the WCR. The WCE was calculated by the ratio of WCR and the mass of evaporated water.

The long-term solar desalination was conducted in an intermittent operation mode[49]. The ion concentrations in the seawater (from the East China Sea) and condensed water were measured by inductively coupled plasma optical emission spectroscopy (ICP-OES 730, Agilent). The wastewater treatment experiments were conducted in the industrial dyeing wastewater and urban domestic sewage (from Changsha Water Industry Group Co., Ltd). The pristine wastewater and

condensed water were evaluated by the COD, TOC, and TDS value. The removal ratio (φ) of COD, TOC, and TDS was calculated by Eq. (6) where S_0 and S_t were the COD, TOC, or TDS value of the original wastewater and condensed water, respectively.

$$\varphi = \frac{S_0 \text{-} S_t}{S_0} \tag{6}$$

Nitrate adsorption measurement

Except for the cyclic adsorption-desorption experiments, all nitrate adsorption experiments can be considered continuous operation processes. Unless investigating the effect of adsorption conditions (temperature, concentration, pH, etc.) on adsorption performance, the uniform initial conditions for all adsorption experiments were as follows: the initial concentration of nitrate solution is 30 ppm; the initial adsorption temperature is 25°C; the initial pH is 7. For the nitrate adsorption experiments under lightless conditions, the samples (BCBH/PPy and BCBH) were immersed into an appropriate amount of sodium nitrate solution. The adsorption experiments were conducted under static conditions for 24 h to ensure adsorption saturation. After the designated adsorption time, the solution was filtered through a 0.22 μm filter membrane. The residual nitrate concentration in the solution was measured using ion chromatography (Dionex, ICS-5000+, USA). The nitrate adsorption capacity was calculated using Eq. (7).

$$q = \frac{(C_0 \text{-} C_t)}{S} \times V \tag{7}$$

Where q (g m^{-2}) was the adsorption capacity; C_0 (mg L^{-1}) was the initial concentration of nitrate; C_t (mg L^{-1}) was the residual nitrate concentration after adsorption; V (L) was the volume of the sodium nitrate solution; and S (m^2) was the sample area. The adsorption ratio (AR) was calculated based on Eq. (8):

$$AR = \frac{C_0 \text{-} C_t}{C_0} \tag{8}$$

For the nitrate adsorption experiments under solar irradiation, the solution below BPEP was sodium nitrate solution. The measured scheme was similar to the dark-field adsorption experiment. The cyclic adsorption performance was evaluated through batch experiments with the following initial conditions: nitrate concentration was 30 ppm, adsorption temperature was 25°C, and solar

flux was 1 sun. The operating time of each adsorption experiment was set to 24 h. After each cycle test, the BCBH/PPy was removed from the BPEP and then soaked in a 10 wt% KCl solution, followed by 12 h of shaking. Afterward, the BCBH/PPy was washed with deionized water to neutralize it and then placed back into BPEP for conducting further adsorption experiments.

The relative contributions of various factors to enhanced nitrate adsorption under solar irradiation were quantitatively assessed as follows[26,27]:

$$ED_i = \frac{q_i \text{-} q_d}{q_s \text{-} q_d} \qquad (9)$$

Where ED_i was contribution of each factor to enhanced nitrate adsorption; q_i was the adsorption capacity in the dark under different conditions (such as varying concentration or temperature); q_s was the adsorption capacity under solar irradiation; q_d was the adsorption capacity in the dark at 25°C. The contribution of the flowing field to enhanced nitrate adsorption was calculated using Eq. (10) where ED_F, ED_T, and ED_C were the contributions of the flowing field, temperature field, and concentration field.

$$ED_F = 100\% \text{-} ED_T \text{-} ED_C \qquad (10)$$

The nitrate adsorption capacity in outdoor experiments was calculated by Eq. (7).

Data Availability

The data that supports the findings of the study are included in the main text and supplementary information files. Source data are provided with this paper.

References

1   Headey, D. & Ruel, M. Food inflation and child undernutrition in low and middle income countries. *Nat. Commun.* **14**, 5761 (2023).

2   Hu, A. *et al.* Highly efficient solar steam evaporation via elastic polymer covalent organic frameworks monolith. *Nat. Commun.* **15**, 9484 (2024).

3   Moriyama, N. *et al.* Steam recovery from flue gas by organosilica membranes for simultaneous harvesting of water and energy. *Nat. Commun.* **14**, 7641 (2023).

4   Zhou, H. *et al.* Solar-driven drum-type atmospheric water harvester based on bio-based gels with fast adsorption/desorption kinetics. *Adv. Mater.* **36**, 2403876 (2024).

5   Li, J. *et al.* A photosynthetically active radiative cooling film. *Nat. Sustain.* **7**, 786-795 (2024).

6   Zhang, W. *et al.* Assessing global drinking water potential from electricity-free solar water evaporation device. *Nat. Commun.* **15**, 6784 (2024).

7   Perez, N. *et al.* Ending groundwater overdraft without affecting food security. *Nat. Sustain.* **7**, 1007-1017 (2024).

8   Podgorski, J. *et al.* Groundwater vulnerability to pollution in Africa's Sahel region. *Nat. Sustain.* **7**, 558-567 (2024).

9   Li, T. *et al.* Sulfate-enabled nitrate synthesis from nitrogen electrooxidation on a rhodium electrocatalyst. *Angew. Chem. Int. Ed.* **61**, e202204541 (2022).

10   Chen, J. G. *et al.* Beyond fossil fuel–driven nitrogen transformations. *Science* **360**, eaar6611 (2018).

11   Seh, Z. W. *et al.* Combining theory and experiment in electrocatalysis: Insights into materials design. *Science* **355**, eaad4998 (2017).

12   Zhai, S. *et al.* Control of particulate nitrate air pollution in China. *Nat. Geosci.* **14**, 389-395 (2021).

13   Wang, J., Liu, X., Beusen, A. H. W. & Middelburg, J. J. Surface-water nitrate exposure to world populations has expanded and intensified during 1970-2010. *Environ. Sci. Technol.*

57, 19395-19406 (2023).

14   Chen, S. *et al.* Direct electroconversion of air to nitric acid under mild conditions. *Nat. Synth.* **3**, 76-84 (2024).

15   Service, R. F. Liquid sunshine. *Science* **361**, 120-123 (2018).

16   Chen, J. G. *et al.* Beyond fossil fuel–driven nitrogen transformations. *Science* **360**, eaar6611 (2018).

17   Hu, Q. *et al.* Pulsed co-electrolysis of carbon dioxide and nitrate for sustainable urea synthesis. *Nat. Sustain.* **7**, 442-451 (2024).

18   Liu, C. *et al.* Electrocatalytic nitrate reduction using iron single atoms for sustainable ammonium supplies to increase rice yield. *Proc. Natl. Acad. Sci.* **121**, e2408187121 (2024).

19   He, D. *et al.* Regulation of the electrocatalytic nitrogen cycle based on sequential proton-electron transfer. *Nat. Catal.* **5**, 798-806 (2022).

20   Yan, Q. *et al.* Enhancing compatibility of two-step tandem catalytic nitrate reduction to ammonia over P-Cu/Co(OH)$_2$. *Adv. Mater.* **36**, 2408680 (2024).

21   Ren, Y., You, S., Wang, Y., Yang, J. & Liu, Y. Bioinspired tandem electrode for selective electrocatalytic synthesis of ammonia from aqueous nitrate. *Environ. Sci. Technol.* **58**, 2144-2152 (2024).

22   Kim, K. *et al.* Coupling nitrate capture with ammonia production through bifunctional redox-electrodes. *Nat. Commun.* **14**, 823 (2023).

23   Kim, K.-H. *et al.* Energy-efficient electrochemical ammonia production from dilute nitrate solution. *Energy Environ. Sci.* **16**, 663-672 (2023).

24   Chen, J. *et al.* Eggshell membrane derived nitrogen rich porous carbon for selective electrosorption of nitrate from water. *Water Res.* **216**, 118351 (2022).

25   Mao, K., Zhang, Y. & Tan, S. C. Functionalizing solar-driven steam generation towards water and energy sustainability. *Nat. Water* **3**, 144-156 (2025).

26   Zhu, L. *et al.* Solar-powered hierarchical microenvironments with authigenic multi-field synergies for simultaneous extraction of freshwater and cesium. *Adv. Sci.*, 2505997 (2025)

27   Li, L. *et al.* Hierarchical photothermal network spontaneously facilitates co-extraction of clean water and boron. *Adv. Funct. Mater.* **42**, 2505776 (2025).

28   Pu, Y. *et al.* Large-scale 3D printed fouling-resistant self-floating evaporator. *Nat. Commun.* **16**, 3677 (2025).

29   Song, Y., Fang, S., Xu, N. & Zhu, J. Solar-driven interfacial evaporation technologies for food, energy and water. *Nat. Rev. Clean Technol.* **1**, 55-74 (2025).

30   Xiang, W., Yu, Z., Zhao, C., Xu, Z. & Zhang, Y. Solar-powered selective mineral extraction via interfacial photothermal evaporation for sustainable lithium supply. *Carbon Neutral.* **4**, 17 (2025).

31   Xu, S. *et al.* Ion pump-inspired biomimetic interfacial evaporation platform for simultaneous seawater desalination, uranium extraction, and electricity generation. *Nano Energy* **131**, 110232 (2024).

32   Mohsenipour, M., Shahid, S. & Ebrahimi, K. Nitrate Adsorption on Clay Kaolin: Batch Tests. *J. Chem.* **2015**, 397069 (2015).

33   Gouran-Orimi, R., Mirzayi, B., Nematollahzadeh, A. & Tardast, A. Competitive adsorption of nitrate in fixed-bed column packed with bio-inspired polydopamine coated zeolite. *J. Environ. Chem. Eng.* **6**, 2232-2240 (2018).

34   Hekmatzadeh, A. A., Karimi-Jashni, A., Talebbeydokhti, N. & Kløve, B. Adsorption kinetics of nitrate ions on ion exchange resin. *Desalination* **326**, 125-134 (2013).

35   Eltaweil, A. S. *et al.* Chitosan based adsorbents for the removal of phosphate and nitrate: A critical review. *Carbohydr. Polym.* **274**, 118671 (2021).

36   Liu, Y., Zhang, X. & Wang, J. A critical review of various adsorbents for selective removal of nitrate from water: Structure, performance and mechanism. *Chemosphere* **291**, 132728 (2022).

37   Priya, E., Kumar, S., Verma, C., Sarkar, S. & Maji, P. K. A comprehensive review on technological advances of adsorption for removing nitrate and phosphate from waste water. *J. Water Process Eng.* **49**, 103159 (2022).

38   Li, H. *et al.* Polypyrrole-modified mushroom residue activated carbon for sulfate and nitrate removal from water: Adsorption performance and mechanism. *J. Water Process Eng.* **49**, 102916 (2022).

39   Li, J. *et al.* Positive feed-forward regulation of nitrate uptake by rice roots and its molecular mechanism. *Sci. Rep.* **14**, 17284 (2024).

40   Yu, Z. *et al.* Micro-Nano Water Film Enabled High-Performance Interfacial Solar Evaporation. *Nano-Micro Lett.* **15**, 214 (2023).

41   Yu, Z. *et al.* High-flux flowing interfacial water evaporation under multiple heating sources enabled by a biohybrid hydrogel. *Nano Energy* **98**, 107287 (2022).

42   Boota, M. *et al.* Pseudocapacitive electrodes produced by oxidant-free polymerization of pyrrole between the layers of 2D titanium carbide (MXene). *Adv. Mater* **28**, 1517-1522 (2016).

43   de Lima, L. F. *et al.* An investigation of the synergistic effect between magnetite nanoparticles and polypyrrole in nanostructured layer-by-layer films. *J. Appl. Polym. Sci.* **138**, 49750 (2021).

44   Yang, L., Lahiri, A., Krebs, F. & Endres, F. Zinc storage mechanism in polypyrrole electrodeposited from aqueous, organic, and ionic liquid electrolytes: an in situ raman spectroelectrochemical study. *ACS Appl. Energy Mater.* **5**, 3217-3226 (2022).

45   Zhao, C. *et al.* Re-stickable yarn supercapacitors with vaper phase polymerized multi-layered polypyrrole electrodes for smart garments. *Macromol. Rapid Commun.* **43**, 2200347 (2022).

46   Feng, J.-X. *et al.* Silica-polypyrrole hybrids as high-performance metal-free electrocatalysts for the hydrogen evolution reaction in neutral media. *Angew. Chem. Int. Ed.* **56**, 8120-8124 (2017).

47   Bi, S., Hou, L. & Lu, Y. Multifunctional sodium alginate fabric based on reduced graphene oxide and polypyrrole for wearable closed-loop point-of-care application. *Chem. Eng. J.* **406**, 126778 (2021).

48   Yu, Z. *et al.* Microplastic detection and remediation through efficient interfacial solar evaporation for immaculate water production. *Nat. Commun.* **15**, 6081 (2024).

49   Yu, Z. *et al.* Polymeric solid wastes for efficient and stable solar desalination and the outdoor clean water production performance prediction. *Sep. Purif. Technol.* **301**, 121938 (2022).

50   Sharqawy, M. H., Lienhard, J. H. & Zubair, S. M. Thermophysical properties of seawater: a review of existing correlations and data. *Desal. Water Treat.* **16**, 354-380 (2010).

51   Wang, H. *et al.* Facile synthesis of polypyrrole decorated reduced graphene oxide-Fe_3O_4 magnetic composites and its application for the Cr(VI) removal. *Chem. Eng. J.* **262**, 597-606 (2015).

52   Wei, M. *et al.* Study on the Photochromism of Ni-Al Layered Double Hydroxides Containing Nitrate Anions. *Eur. J. Inorg. Chem.* **2006**, 2831-2838 (2006).

53   Sun, Y. & Zheng, W. Polyethylenimine-functionalized polyacrylonitrile anion exchange fiber as a novel adsorbent for rapid removal of nitrate from wastewater. *Chemosphere* **258**, 127373 (2020).

54   Wang, J.-G., Liu, H., Liu, H., Hua, W. & Shao, M. Interfacial constructing flexible V_2O_5@polypyrrole core-shell nanowire membrane with superior supercapacitive performance. *ACS Appl. Mater. Interfaces* **10**, 18816-18823 (2018).

55   Godiya, C. B., Ruotolo, L. A. M. & Cai, W. Functional biobased hydrogels for the removal of aqueous hazardous pollutants: current status, challenges, and future perspectives. *J. Mater. Chem. A* **8**, 21585-21612 (2020).

56   Ducker, W. A. Decreasing the energy of evaporation using interfacial water: is this useful for solar evaporation efficiency? *ACS Omega* **8**, 19705-19707 (2023).

57   Zhang, J. H., Mittapally, R., Lv, G. & Chen, G. Superthermal solar interfacial evaporation is not due to reduced latent heat of water. *Energy Environ. Sci.* **18**, 1707-1721 (2025).

58   Yu, Z. *et al.* Interfacial solar evaporator for clean water production and beyond: From design to application. *Appl. Energy* **299**, 117317 (2021).

59   Liu, X. *et al.* 3D hydrogel evaporator with vertical radiant vessels breaking the trade-off between thermal localization and salt resistance for solar desalination of high-salinity. *Adv. Mater.* **34**, 2203137 (2022).

60   Cui, L. *et al.* Rationally constructing a 3D bifunctional solar evaporator for high-performance water evaporation coupled with pollutants degradation. *Appl. Catal. B: Environ.* **337**, 122988 (2023).

61   Ye, J. *et al.* Wastewater denitrification driven by mechanical energy through cellular piezo-sensitization. *Nat. Water* **2**, 531-540 (2024).

62   Jia, S. *et al.* Upgrading of nitrate to hydrazine through cascading electrocatalytic ammonia production with controllable N-N coupling. *Nat. Commun.* **15**, 8567 (2024).

63   Pan, Y. *et al.* Electrocatalytic coupling of nitrate and formaldehyde for hexamethylenetetramine synthesis via c–n bond construction and ring formation. J. Am. Chem. Soc. **146**, 19572-19579 (2024).

64   Xiong, Y. *et al.* Effects of expanded graphite on $NaNO_3$/semi-coke ash shape-stable phase change composites for thermal energy storage. *J. Energy Storage* **72**, 108648 (2023).

65   Huang, W. *et al.* Cascade electrocatalytic nitrate reduction reaching 100% Nitrate-N to Ammonia-N conversion over Cu_2O@CoO yolk-shell nanocubes. *ACS Nano* **18**, 20258-20267 (2024).

66   Huang, D.-S. *et al.* Electrosynthesis of urea by using Fe_2O_3 nanoparticles encapsulated in a conductive metal–organic framework. *Nat. Synth.* **3**, 1404-1413 (2024).

67   Bian, J. *et al.* Directional electron transfer in enzymatic nano-bio hybrids for selective photobiocatalytic conversion of nitrate. *Angew. Chem. Int. Ed.* **136**, e202412194 (2024)

68   Huang, Y. *et al.* Pulsed electroreduction of low-concentration nitrate to ammonia. *Nat. Commun.* **14**, 7368 (2023).

69   Chen, F.-Y. *et al.* Efficient conversion of low-concentration nitrate sources into ammonia on a Ru-dispersed Cu nanowire electrocatalyst. *Nat. Nanotechnol.* **17**, 759-767 (2022).

70   Li, L., Su, Y., Jin, B., Yu, Z. & Cheng, S. Recycling waste carbon fibers for solar-driven

clean water production by one-step electrochemical process. *Sep. Purif. Technol.* **351**, 128019 (2024).

71   Yu, Z. *et al.* Enhanced interfacial solar evaporation through formation of micro-meniscuses and microdroplets to reduce evaporation enthalpy. *Adv. Funct. Mater.* **32**, 2108586 (2022).

72   Li, X. *et al.* Measuring conversion efficiency of solar vapor generation. *Joule* **3**, 1798-1803 (2019).

73   Tang, J. *et al.* Realization of low latent heat of a solar evaporator via regulating the water state in wood channels. *ACS Appl. Mater. Interfaces* **12**, 18504-18511 (2020).

74   Zhao, F. *et al.* Highly efficient solar vapour generation via hierarchically nanostructured gels. *Nat. Nanotechnol.* **13**, 489-495 (2018).

75   Vu, C. T. & Wu, T. MgAl-layered double hydroxides/sodium alginate beads for nitrate adsorption from groundwater and potential use as a slow-release fertilizer. *J. Clean. Prod.* **379**, 134508 (2022).

76   Homagai, P. L., Poudel, R., Paudyal, H., Ghimire, K. N. & Bhattarai, A. Adsorption of nitrate and nitrite anion by modified maize stalks from aqueous solutions. *Environ. Sci. Pollut. Res.* **30**, 54682-54693 (2023).

77   El Kaim Billah, R. *et al.* Experimental and theoretical studies on nitrate removal using epichlorohydrin-modified cross-linked chitosan derived from shrimp waste. *Environ. Sci. Pollut. Res.* **30**, 107772-107789 (2023).

78   Bhoi, B. & Chandra, V. Innovative $BiVO_4$/MXene nanocomposite for efficient nitrate adsorption. *J. Environ. Chem. Eng.* **13**, 117621 (2025).

79   Song, W. *et al.* Adsorption of nitrate from aqueous solution by magnetic amine-crosslinked biopolymer based corn stalk and its chemical regeneration property. *J. Hazard. Mater.* **304**, 280-290 (2016).
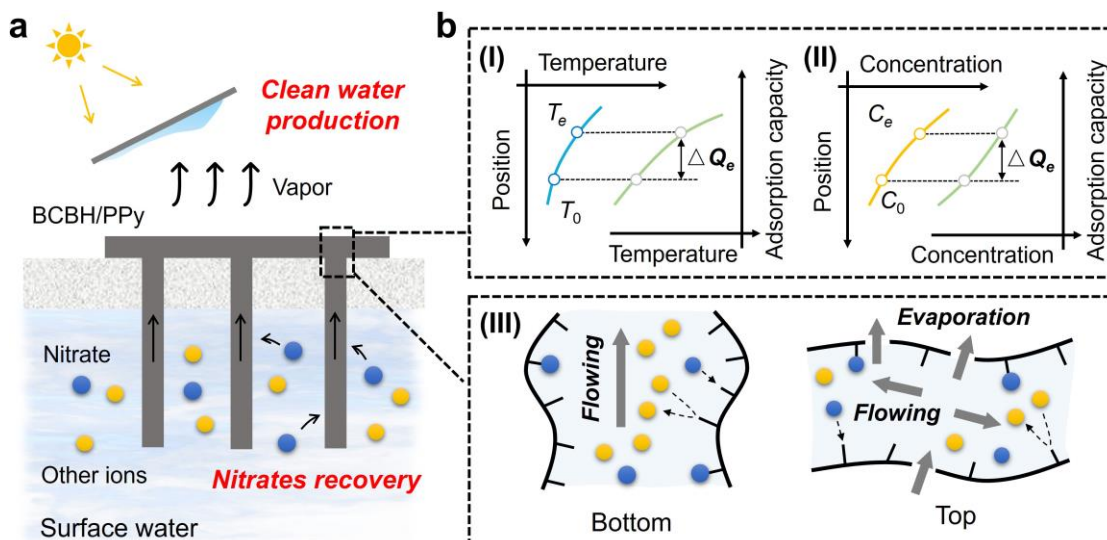
Acknowledgments

Author Contributions Statement

These authors contributed equally: Zhen Yu, Lei Shi. Z. Y., L. S., and S. C. T. conceived and designed the project. Z. Y., R. N., and H. H. conducted the experiments. Z. S., J. C., and T. Z. contributed to the theoretical analysis and theoretical calculations. Z. Y. and L. S. organized the data and wrote the manuscript. S. C. T. polished the manuscript. All authors discussed the results and approved the final version of the manuscript.

Competing Interests Statement
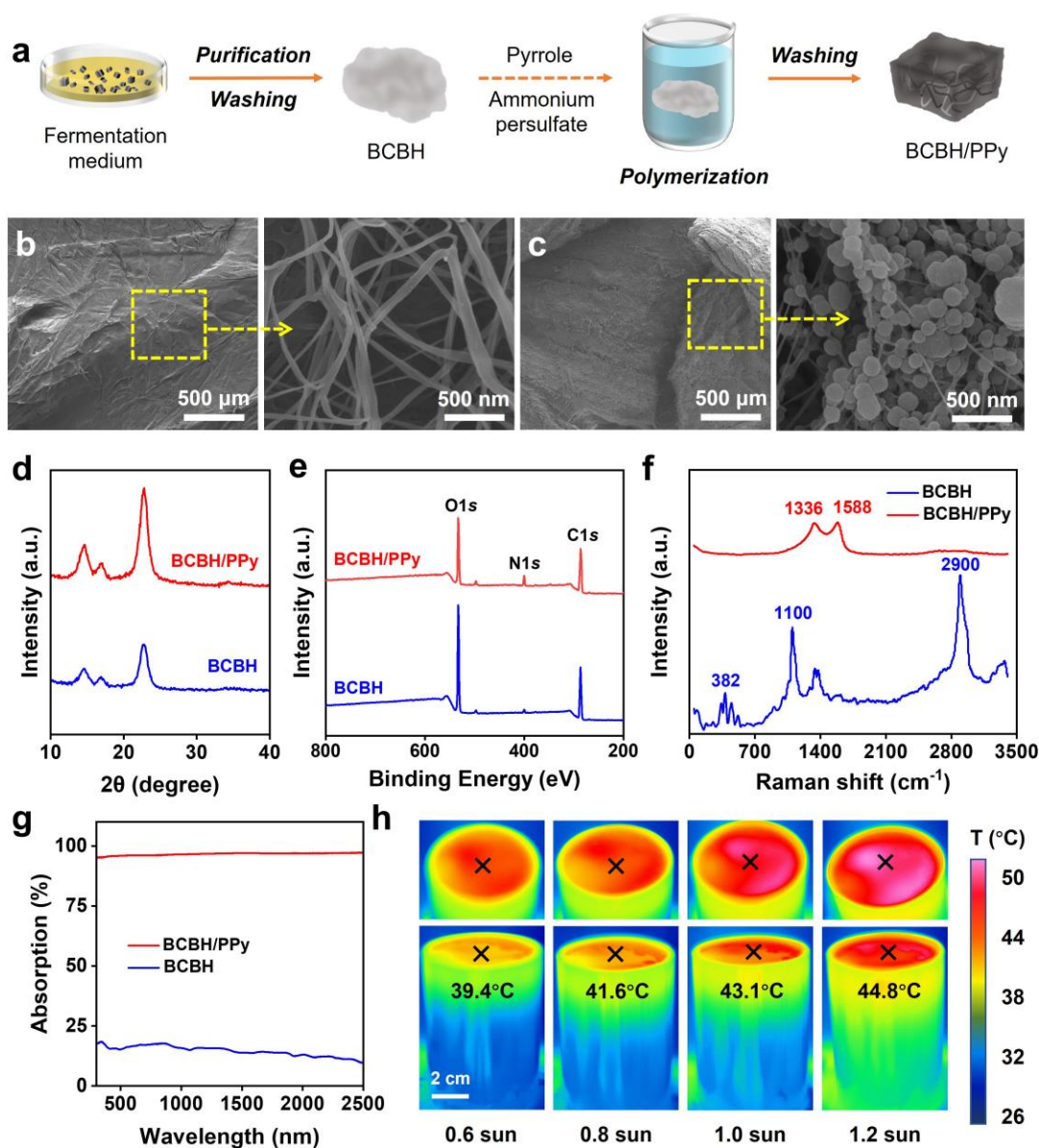
The authors declare no competing interests.

Figure Legends/Captions

Fig. 1 | The design inspiration of BPEP

a, Schematic diagram of BPEP recovering nitrate and producing clean water under light conditions.

b, Evaporation-induced multi-field enhanced nitrate recovery mechanism: (I) Temperature field; (II) Concentration field; and (III) Flowing field. The value of each physical quantity increased along the direction of the arrow. T_0-initial temperature; T_e-evaporation interface temperature; C_0-initial concentration; C_e-evaporation interface concentration; ΔQ_e-adsorption capacity increment.

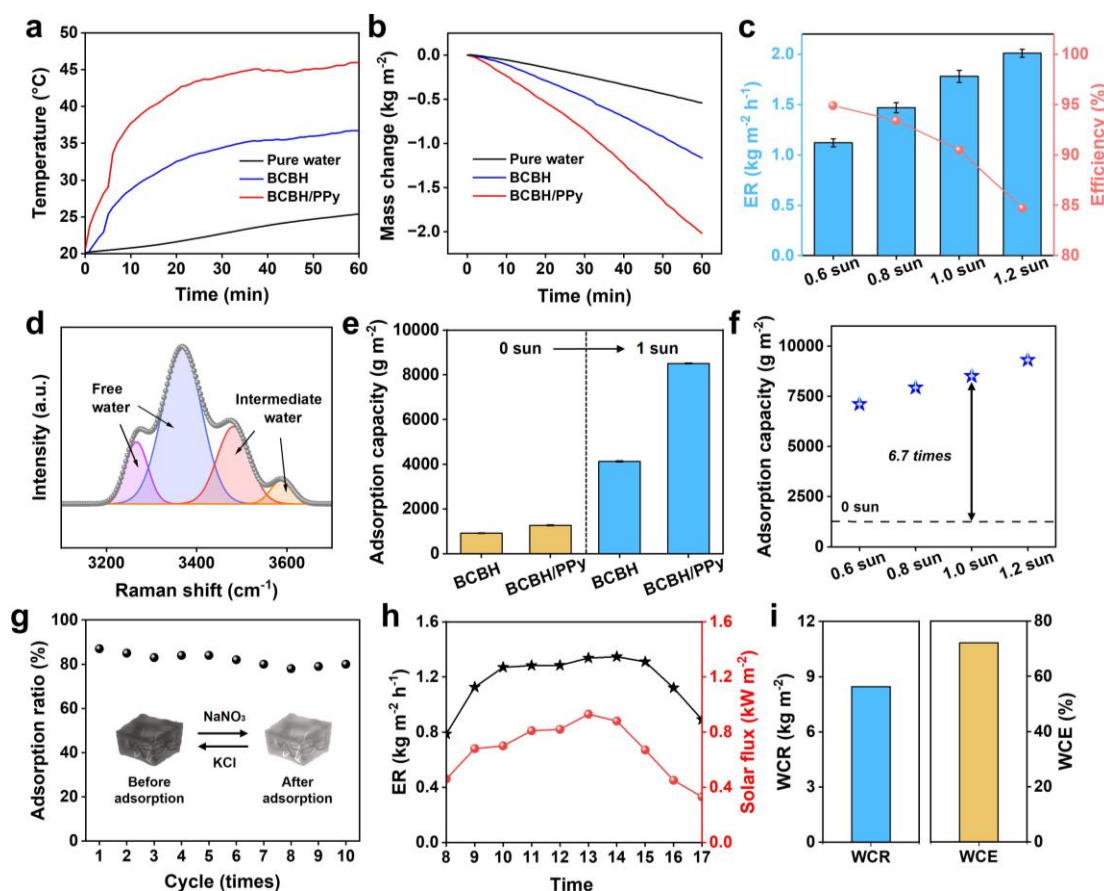**Fig. 2. Fabrication and characteristics of BCBH and BCBH/PPy**

a, Schematic diagram of the fabrication process.

b, SEM images of BCBH.

c, SEM images of BCBH/PPy.

d, XRD patterns; **e,** XPS curves; **f,** Raman curves; and **g,** The UV-Vis-NIR adsorption spectra of BCBH and BCBH/PPy.

h, The IR photos of BPEP under different solar fluxes.

Fig. 3 | The solar-driven evaporation and nitrate recovery performance

a, The temperature rising curves of pure water, BCBH and BCBH/PPy under 1.2 sun.

b, The mass change curves of pure water, BCBH and BCBH/PPy under 1.2 sun.

c, The evaporation rate (ER) and efficiency of BPEP under different solar fluxes. Error bars represent the standard deviations from three-time measurements.
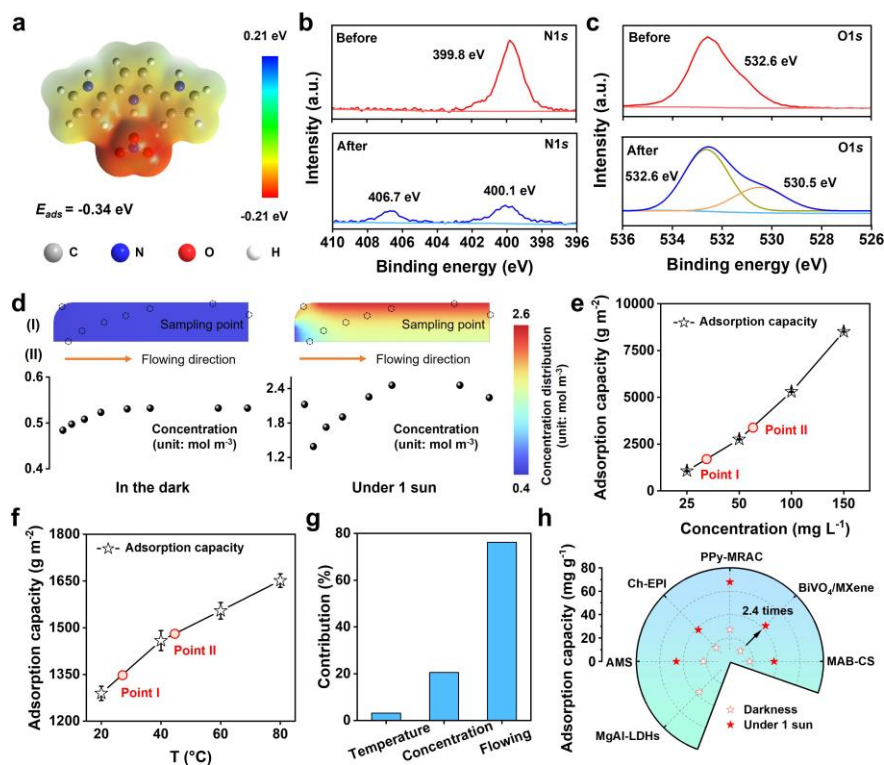
d, Raman curves of BCBH/PPy.

e, The nitrate adsorption capacity of BPEP under different conditions. Error bars represent the standard deviations from three-time measurements.

f, The nitrate adsorption capacity of BPEP under different solar fluxes. Error bars represent the standard deviations from three-time measurements.

g, The cyclic nitrate adsorption ratio. Inset: Cyclic adsorption process of nitrates by BPEP.

h, The evaporation rate and solar flux in outdoor experiments.

i, The WCR and WCE in outdoor experiments.

Fig. 4 | The enhanced nitrate recovery mechanism

a, The surface electrostatic potential distribution and adsorption energy between PPy and nitrate.

b, N1s and **c,** O1s spectra of the BCBH/PPy before and after nitrate adsorption.

d, The nitrate adsorption simulation by COMSOL software: I-The concentration distribution of nitrate on BPEP under 1 sun illumination and dark conditions following adsorption. The 'flowing direction' represents the direction of solution flow, and the 'sampling point' represents a randomly distributed point. II-The nitrate concentration of the sample points on BPEP under 1 sun illumination and dark conditions following adsorption.
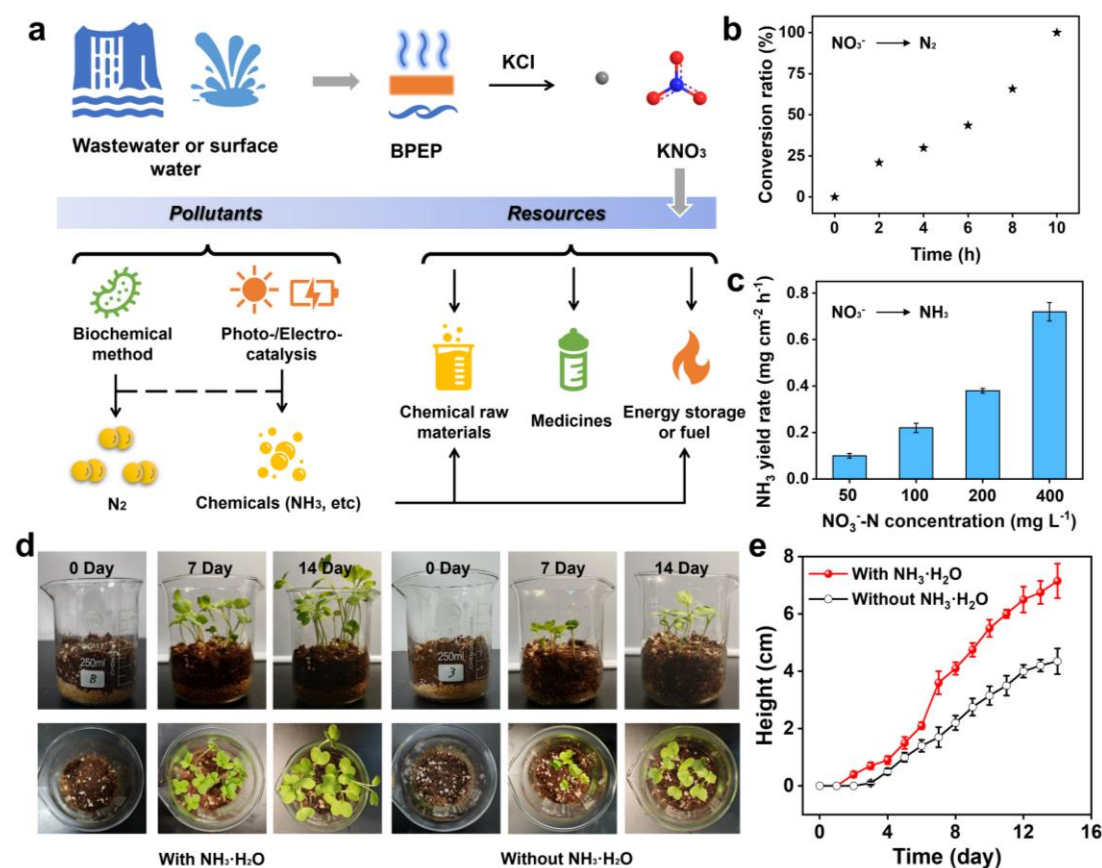
e, The nitrate adsorption capacity of BPEP under different initial nitrate concentrations in the dark. The conditions at the evaporation interface before illumination are marked as point I, whereas those after illumination are marked as point II in Fig. 4e and Fig. 4f. Error bars represent the standard deviations from three-time measurements.

f, The nitrate adsorption capacity of BPEP under different concentrations in the dark. Error bars represent the standard deviations from three-time measurements.

g, The contribution of various factors in enhancing nitrate recovery under 1 sun.

h, The nitrate recovery capacity of BPEP based on other reported adsorbents under 1 sun: MgAl-LDHs[75]; AMS[76]; Ch-EPI[77]; PPy-MRAC[38]; BiVO$_4$/MXene[78]; MAB-CS[79].

Fig. 5 | Discussion on BPEP

a, Resource utilization pathway of nitrate based on BPEP.

b, Nitrate conversion in sequencing batch reactor.

c, Ammonia (NH$_3$) yield rate under different concentrations of nitrate. Noted that the ammonia was produced electrochemically from the recovered nitrate by BPEP. Error bars represent the standard deviations from three-time measurements.

d, The height changes of the *Pakchoi* in its growing process with or without fabricated ammonia solution added.

e, The digital photos of the *Pakchoi* in its growing process with or without fabricated ammonia solution added.

Editorial Summary:

Recovering nitrate from surface water can help address interconnected environmental, resource, and energy challenges. A bioinspired photothermal evaporation platform enabling the co-recovery of low-concentration nitrate and freshwater is proposed.

Peer review information: *Nature Communications* thanks Zonglu Yao, and the other, anonymous, reviewer(s) for their contribution to the peer review of this work. A peer review file is available.